Peer reviewed:

No

Title:

Skeleton-stabilized ImmersoGeometric Analysis for incompressible viscous flow problems

Author:

Tuong Hoang[1,2], Clemens V. Verhoosel[1], Chao-Zhong Qin[1], Ferdinando Auricchio[3], Alessandro Reali[3,4], E. Harald van Brummelen[1]

1. Eindhoven University of Technology, Department of Mechanical Engineering, The Netherlands
2. IUSS - Istituto Universitario di Studi Superiori, Pavia, Italy
3. University of Pavia, Department of Civil Engineering and Architecture, Pavia, Italy
4. Technische Universitat Munchen - Institute for Advanced Study, Garching, Germany

Publication date:

12-2017

Copyright information:

Skeleton-stabilized ImmersoGeometric Analysis for incompressible viscous flow problems

Tuong Hoang[a,b,*], Clemens V. Verhoosel[a], Chao-Zhong Qin[a], Ferdinando Auricchio[c], Alessandro Reali[c,d], E. Harald van Brummelen[a]

[a] *Eindhoven University of Technology – Department of Mechanical Engineering, P.O. Box 513, 5600MB Eindhoven, The Netherlands*

[b] *IUSS – Istituto Universitario di Studi Superiori Pavia, 27100 Pavia, Italy*

[c] *University of Pavia – Department of Civil Engineering and Architecture, 27100 Pavia, Italy*

[d] *Technische Universität München – Institute for Advanced Study, 85748 Garching, Germany*

Abstract

A Skeleton-stabilized ImmersoGeometric Analysis technique is proposed for incompressible viscous flow problems with moderate Reynolds number. The proposed formulation fits within the framework of the finite cell method, where essential boundary conditions are imposed weakly using a Nitsche-type method. The key idea of the proposed formulation – which was considered in the conforming isogeometric analysis setting by Hoang *et.al.* [1] – is to stabilize the jumps of high-order derivatives of variables over the skeleton of the background mesh. The formulation allows the use of identical finite-dimensional spaces for the approximation of the pressure and velocity fields in immersed domains. The stability issues observed for inf-sup stable discretizations of immersed incompressible flow problems [2] are avoided with this formulation. For B-spline basis functions of degree k with highest regularity, only the derivative of order k has to be controlled, which requires specification of only a single stabilization parameter. The Stokes and Navier-Stokes equations are studied numerically in two and three dimensions using various immersed test cases. Oscillation-free solutions and optimal convergence rates can be obtained.

Keywords: Isogeometric analysis, Immersogeometric analysis, Skeleton-stabilization, Embedded domain method, XFEM, CutFEM, Finite cell method, Stokes, Navier-Stokes, Stabilization

1. Introduction

Finite Element Analysis (FEA) of incompressible flow problems has been an active topic of research over the last decades, with research interests ranging from theoretical aspects to engineering applications. In recent years, IsoGeometric Analysis (IGA) – a spline-based finite element simulation paradigm proposed by Hughes *et al.* [3] with the aim of establishing a better integration between Computer-Aided Design (CAD) and FEA – has been studied in the context of incompressible flow problems. Isogeometric analysis of mixed formulations for incompressible flow problems based on *inf-sup* stable velocity-pressure pairs has been studied in detail in the literature, which has led to the

*Corresponding author.
Email addresses:
tuong.hoang@iusspavia.it, t.hoang@tue.nl (T. Hoang)
c.v.verhoosel@tue.nl (C.V. Verhoosel),
c.qin@tue.nl (C. Qin),
auricchio@unipv.it (F. Auricchio),
alessandro.reali@unipv.it (A. Reali)
e.h.v.brummelen@tue.nl (E.H. van Brummelen)

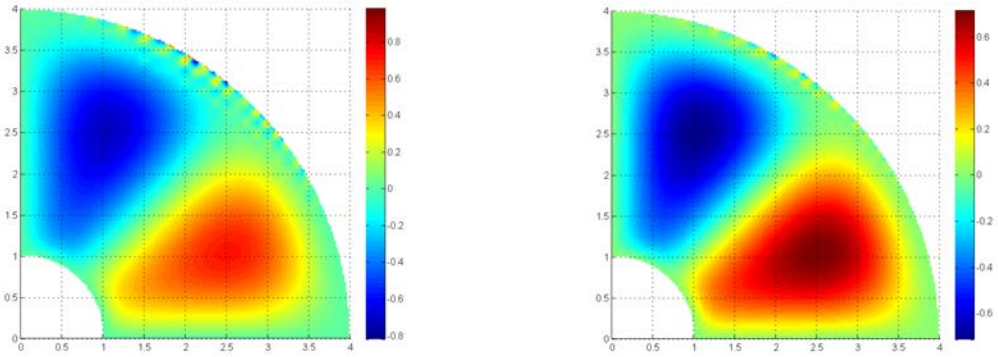

(a) (b)

Figure 1: Unphysical pressure oscillations are observed when the Stokes problem is solved in the standard finite cell setting using *(a)* inf-sup stable isogeometric elements, shown here for Taylor-Hood (see Ref. [2] for details), and *(b)* using a Galerkin Least-squares method.

development of a range of isogeometric element families, namely: Taylor-Hood elements [4–6], Subgrid elements [6, 7], H(div)-conforming elements [5, 8–10], and Nédélec elements [5]. These element families have been demonstrated to be suitable for the discretization of incompressible flow problems, by virtue of the fact that they leverage the advantageous mathematical properties of the spline basis functions used in isogeometric analysis [11].

The Finite Cell Method (FCM) – an immersed finite element method introduced by Rank *et al.* [12] – has been found to be a natural companion to isogeometric analysis. The key idea of the FCM is to embed a geometrically complex physical domain of interest into a geometrically simple embedding domain, on which a regular mesh can be built easily. The framework in which IGA and FCM are integrated – first considered by Schillinger, Rank *et al.* [13–15] – is also referred to as immersogeometric analysis [16, 17]. On the one hand immersogeometric analysis facilitates consideration of CAD trimming curves in the context of isogeometric analysis. On the other hand, it enables the construction of high-regularity spline spaces over geometrically and topologically complex volumetric domains, for which analysis-suitable spline parametrizations are generally not available. The isogeometric finite cell method has been applied to various problems in solid and structural mechanics (see [18, 19] for comprehensive reviews), in image-based analysis [20, 21], in fluid-structure interaction problems [16, 17], and in various other application areas.

In Hoang *et.al* [2] we have found that when the inf-sup stable isogeometric element families for incompressible flow problems are applied in the finite cell setting, local pressure oscillations generally occur in the vicinity of cut boundaries. An illustration of this oscillatory behavior is shown in Figure 1a. When employing the Galerkin-Least square (GLS) method, we observe similar behavior, as shown in Figure 1b. The occurrence of such oscillations on cut elements with relatively large volume fractions implies that this problem is related to the inf-sup stability of the discrete problem, rather than to conditioning issues related to cut elements with small volume fractions. It is important to note that although the inf-sup stable discretization pairs (and GLS) lead to close-to-optimal converge behavior of global error measures, the oscillations in the pressure field near the immersed boundaries persist under mesh refinement. As a consequence, the approximation of quantities of interest related to the immersed boundaries is below standard, which makes the inf-sup stable (and GLS) isogeometric approach less attractive for a large class of immersed incompressible flow problems.

In this manuscript we propose an alternative formulation – based on the skeleton-based stabilization technique developed by Hoang *et.al* [1] in the context of conforming isogeometric analysis – to resolve the stability problems associated with immersed inf-sup isogeometric discretization pairs. In this formulation – which can be regarded as a high-regularity generalization of the continuous interior penalty method by Burman and Hansbo [22] – we rely on stabilization of the mixed form problem by amending the formulation with a skeleton-based penalty term. This alternative form of stabilization relaxes

the compatibility constraints on the function spaces to be used, which allows us to consider identical discretization spaces for both the velocity and the pressure fields. Our work is related to developments that have been made in the context of XFEM and CutFEM [23–27], and is particularly inspired by the Ghost penalty stabilization technique of Burman and Hansbo [28, 29]. A novelty of our work is that we fully exploit the maximum regularity of the B-spline basis functions used in IGA, as a consequence of which the introduced stabilization operator only acts on the interface jumps of the highest order derivative of the basis functions. As a result we only require a single stabilization term to control both the inf-sup stability of the mixed problem and its related pressure-space conditioning issues. We herein propose to supplement the skeleton-based stabilized formulation in [1] with a ghost-penalty term for the velocity space, which is not required from the inf-sup stability point of view, but which is essential to control the conditioning of the discretized problem.

This paper is outlined as follows. In Section 2 we commence with the introduction of the unsteady incompressible Navier-Stokes equations and the essentials of the finite cell method. In Section 3 we then present the skeleton-stabilized formulation developed and studied in this work. In Section 4 we discuss the algebraic form of of the developed stabilized formulation, and its effect on the sparsity structure of the system to be solved. The proposed formulation is studied by a series of numerical test cases in Section 5, including the case of a three-dimensional image-based analysis of a microstructural porous medium flow. Conclusions are finally presented in Section 6.

2. Preliminaries

Before we introduce the skeleton-based stabilized formulation in Section 3, we here first introduce the problem setting for the unsteady Navier-Stokes equations, and the fundamental concepts of the isogeometric finite cell method.

2.1. The unsteady incompressible Navier-Stokes equations

We consider the unsteady incompressible Navier-Stokes equations on the open bounded domain $\Omega \in \mathbb{R}^d$, where $d = 2, 3$ denotes the spatial dimension of the domain. The Lipschitz boundary $\partial\Omega$ is split in the Dirichlet boundary, Γ_D, and the Neumann boundary, Γ_N, such that $\overline{\Gamma_D} \cup \overline{\Gamma_N} = \partial\Omega$ and $\Gamma_D \cap \Gamma_N = \emptyset$. The unit normal vector to $\partial\Omega$, which points out of the domain, is denoted by $\mathbf{n}$. For any time instant $t \in [0, T)$ the Navier-Stokes equations for the velocity field $\mathbf{u} : \Omega \times [0, T) \to \mathbb{R}^d$ and pressure field $p : \Omega \times [0, T) \to \mathbb{R}$ read:

$$
\left\{
\begin{array}{l}
\text{Find } \mathbf{u} : \Omega \times [0,T) \to \mathbb{R}^d, \text{ and } p : \Omega \times [0,T) \to \mathbb{R} \text{ such that:} \\
\begin{array}{rcll}
\partial_t \mathbf{u} + \nabla \cdot (\mathbf{u} \otimes \mathbf{u}) - \nabla \cdot (2\mu \nabla^s \mathbf{u}) + \nabla p &=& \mathbf{f} & \text{in } \Omega \times (0,T), \\
\nabla \cdot \mathbf{u} &=& 0 & \text{in } \Omega \times (0,T), \\
\mathbf{u} &=& \mathbf{g} & \text{on } \Gamma_D \times (0,T), \\
2\mu \nabla^s \mathbf{u} \cdot \mathbf{n} - p\mathbf{n} &=& \mathbf{h} & \text{on } \Gamma_N \times (0,T), \\
\mathbf{u} &=& \mathbf{u}_0 & \text{in } \Omega \times \{0\}.
\end{array}
\end{array}
\right. \tag{1}
$$

In this problem formulation the symmetric gradient of the velocity field is denoted by $\nabla^s \mathbf{u} := \frac{1}{2}\left(\nabla \mathbf{u} + (\nabla \mathbf{u})^T\right)$ and μ represents the kinematic viscosity. The exogenous data $\mathbf{f} : \Omega \times (0, \infty) \to \mathbb{R}^d$, $\mathbf{g} : \Gamma_D \times (0, \infty) \to \mathbb{R}^d$, and $\mathbf{h} : \Gamma_N \times (0, \infty) \to \mathbb{R}^d$ represent body forces, prescribed velocity, and traction data, respectively. The initial data in the strong form (1) are denoted by $\mathbf{u}_0 : \Omega \to \mathbb{R}^d$.

To provide a framework for the derivation of the immersed formulation introduced in the next section, we here first present the weak formulation in the conforming setting. For any vector space $\mathcal{V}$, we denote by $\mathcal{L}(0, T; \mathcal{V})$ a suitable linear space of $\mathcal{V}$-valued functions on the time interval $(0, T)$. The weak formulation of the initial boundary value problem (1) then follows as:

$$
\left\{
\begin{array}{l}
\text{Find } \mathbf{u} \in \mathcal{L}(0,T; \boldsymbol{\mathcal{V}}_{\mathbf{g},\Gamma_D}) \text{ and } p \in \mathcal{L}(0,T; \mathcal{Q}), \text{ subject to } \mathbf{u}(0) = \mathbf{u}_0, \\
\text{such that for almost all } t \in (0,T): \\
\begin{array}{rcll}
(\partial_t \mathbf{u}, \mathbf{w}) + c(\mathbf{u}; \mathbf{u}, \mathbf{w}) + a(\mathbf{u}, \mathbf{w}) + b(p, \mathbf{w}) &=& \ell_1(\mathbf{w}) & \forall \mathbf{w} \in \boldsymbol{\mathcal{V}}_{\mathbf{0},\Gamma_D}, \\
b(q, \mathbf{u}) &=& 0 & \forall q \in \mathcal{Q}.
\end{array}
\end{array}
\right. \tag{2}
$$

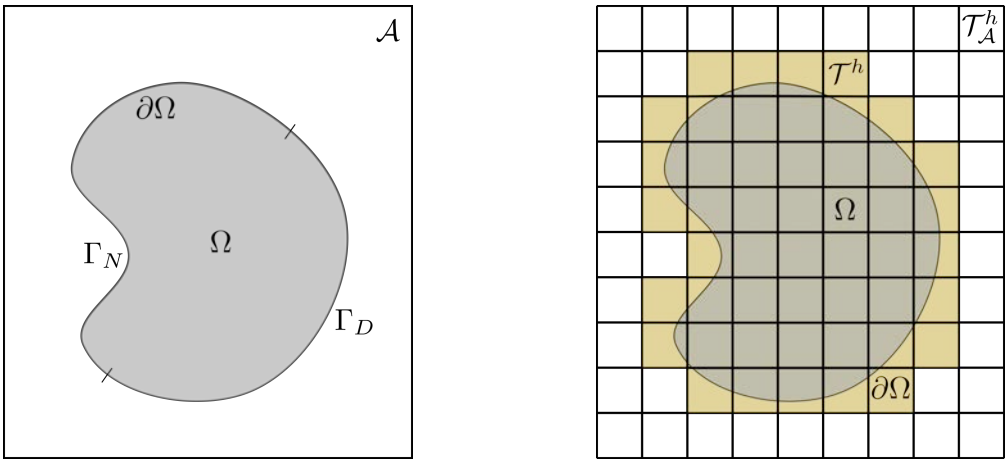

(a) (b)

Figure 2: Schematic representation of *(a)* the physical domain Ω and ambient domain $\mathcal{A}$ as considered in the finite cell method, and *(b)* the ambient domain mesh, $\mathcal{T}_{\mathcal{A}}^h$ (covering the complete ambient domain), and background mesh, $\mathcal{T}^h$ (marked by the yellow background shading).

The linear operators in this formulation are defined as

$$c(\mathbf{v};\mathbf{u},\mathbf{w}) := (\mathbf{v}\cdot\nabla\mathbf{u},\mathbf{w})\,, \tag{3a}$$
$$a(\mathbf{u},\mathbf{w}) := 2\mu\,(\nabla^s\mathbf{u},\nabla^s\mathbf{w})\,, \tag{3b}$$
$$b(q,\mathbf{w}) := -\,(q,\mathrm{div}\mathbf{w})\,, \tag{3c}$$
$$\ell_1(\mathbf{w}) := (\mathbf{f},\mathbf{w}) + \langle\mathbf{h},\mathbf{w}\rangle_{\Gamma_N}\,, \tag{3d}$$

where $(\cdot,\cdot)$ denotes the inner product in $L^2(\Omega)$ and $\langle\cdot,\cdot\rangle_{\Gamma_N}$ denotes the inner product in $L^2(\Gamma_N)$. The function spaces in (2) are defined as

$$\boldsymbol{\mathcal{V}}_{\mathbf{g},\Gamma_D} := \left\{\mathbf{u}\in[H^1(\Omega)]^d : \mathbf{u}=\mathbf{g} \text{ on } \Gamma_D\right\}, \qquad \mathcal{Q} := L^2(\Omega), \tag{4}$$

and the velocity test space, $\boldsymbol{\mathcal{V}}_{\mathbf{0},\Gamma_D}$, is taken as the homogeneous version of $\boldsymbol{\mathcal{V}}_{\mathbf{g},\Gamma_D}$. In the case of pure Dirichlet boundary conditions the pressure is determined up to a constant, which then requires supplementation of the additional pressure condition:

$$\mathcal{Q} := L^2_0(\Omega) \equiv \left\{q\in L^2(\Omega) : \int_\Omega q\,\mathrm{d}\Omega = 0\right\}. \tag{5}$$

2.2. The finite cell method

In the finite cell method, the physical domain of interest, Ω, is immersed into a geometrically simple ambient domain, $\mathcal{A}\supset\Omega$, as illustrated in Figure 2a. In this manuscript we consider the ambient domain to be rectangular, so that it can be partitioned by a regular grid with uniform spacing $h>0$. We refer to this partitioning as the ambient domain mesh, $\mathcal{T}_{\mathcal{A}}^h$. Elements in this ambient domain mesh that do not intersect the physical domain are discarded in the finite cell analysis, which leads to the definition of the finite cell background mesh:

$$\mathcal{T}^h := \{K\in\mathcal{T}_{\mathcal{A}}^h :\ K\cap\Omega\neq\emptyset\} \tag{6}$$

The ambient domain mesh and background mesh are illustrated in Figure 2.

The conceptual idea of the finite cell method is to construct a suitable discretization space on the background mesh, and to use that basis in a Galerkin formulation pertaining to the physical domain. Dirichlet boundary conditions on non-conforming edges are typically enforced weakly, most commonly

by means of Nitsche's method [30]. We will introduce the Nitsche formulation for the problem (1) in Section 3. In the remainder of this section we introduce the B-spline basis defined over the background mesh, and the integration procedure employed to evaluate volume and (immersed) surface integrals over elements that are cut by the immersed boundary.

2.2.1. B-spline basis

By virtue of the fact that in the finite cell method basis functions are constructed on a regular background mesh, it enables the isogeometric analysis of complex-shaped physical domains. In this manuscript we restrict ourselves to a single patch open B-spline basis over the ambient domain mesh, defined by non-decreasing knot vectors in all spatial directions $\delta = 1, \dots, d$,

$$\Xi^{\delta} = [\underbrace{\xi_1^{\delta}, \dots, \xi_1^{\delta}}_{(k+1)-\text{time}}, \xi_2^{\delta}, \dots, \xi_{m^{\delta}-1}^{\delta}, \underbrace{\xi_{m^{\delta}}^{\delta}, \dots, \xi_{m^{\delta}}^{\delta}}_{(k+1)-\text{time}}], \tag{7}$$

In accordance with the definition of open B-splines the first and last knot values are repeated $k+1$ times, where k denotes the global isotropic polynomial degree of the basis. We align the knot vectors with the ambient domain, which essentially implies that the we have an identity geometric map between the parameter domain and the ambient domain. The spacing between two consecutive knots is therefore equal to the global isotropic mesh parameter h.

Using the knot vectors (7) a B-spline basis of degree k can be constructed over the ambient domain by means of the recursive Cox-De Boor formula [31]. We denote this B-spline basis by $\mathcal{N}_{\mathcal{A}}^{k} = \{N_{\mathcal{A},I}^{k} : \mathcal{A} \to \mathbb{R}\}_{I=1}^{n_{\mathcal{A}}}$, where the total number of basis functions is equal to $n_{\mathcal{A}} = \otimes_{\delta=1}^{d}\{m^{\delta} + k - 1\}$, with m^{δ} the number of unique knot values per direction. In the finite cell analysis we discard the basis function that are not supported on the background mesh $\mathcal{T}^h$, so that the B-spline basis follows as:

$$\mathcal{N}^{k} := \{N \in \mathcal{N}_{\mathcal{A}}^{k} : \text{supp}(N) \cap \mathcal{T}^h \neq \emptyset\} \tag{8}$$

Note that, by definition, all basis functions in $\mathcal{N}^k$ have positive support over the physical domain Ω. The cardinality of $\mathcal{N}^k$ is denoted by $n \leq n_{\mathcal{A}}$. We herein consider maximum regularity B-spline bases – as indicated by the non-repeated internal knot values in (7) – so that the basis functions are C^{k-1} continuous. The B-spline function space $\mathcal{S}^k$ spanned by the basis $\mathcal{N}^k$ is therefore a finite dimensional subspace of the Sobolev space $H^k(\Omega^h)$, where $\Omega^h = int(\bigcup_{K \in \mathcal{T}^h} \overline{K})$.

2.2.2. Cut cell integration

For elements in the background mesh that are intersected by the boundaries of the physical domain, standard quadrature rules are inaccurate, since effectively discontinuous functions are integrated over such cut cells. The FCM therefore generally employs an advance numerical-integration technique for cut cells. Herein we use the bisectioning-based segmentation scheme proposed in [21] in the context of the isogeometric finite cell analysis of image-based geometric models, which also enables us to extract a parametrization and quadrature rules for the immersed boundaries.

We illustrate the bisection-based tessellation scheme in Figure 3 for completeness. The element-by-element routine commences with the evaluation of a level set function in the vertices associated with a $\varrho_{\max}$-times uniform refinement of the element. This level set can either be derived from voxel data in a scan-based analysis, or a signed-distance function can be considered in the case that the geometry is provided by a CAD model. The integration points for a cut cell are assembled by traversing the levels of uniform refinement, where for each sub-cell in that level it is determined whether the interface passes through it. If all vertices of a sub-cell exceed a specified threshold value (zero in the case of a signed-distance function) the sub-cell is kept as an integration sub-cell. Otherwise a further subdivision of the sub-cell is considered, and the same check is performed on the next level. On the lowest level this recursion is closed with a tessellation procedure. From an implementation perspective the integration points and weights on all sub-cells are collected on the level of the cut-element, which essentially provides us with an integration scheme tailored to the cut element.

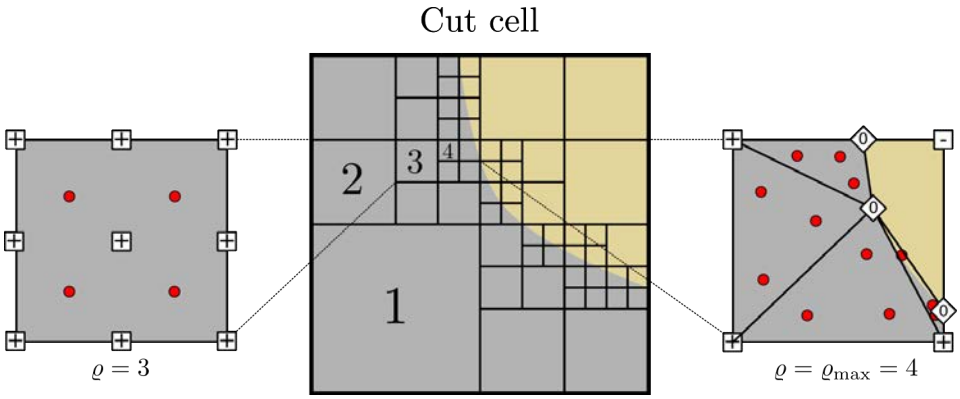

Figure 3: Illustration of the bisection-based tessellation scheme used to generate quadrature rules for the cells that are cut by the immersed boundary. The vertex markers indicate whether the employed interpolant of the level set function is zero (on the boundary), positive (inside the domain), or negative (outside the domain). The red points in the sub-cell zooms are an illustration of the distribution of the integration points in such cells.

The tessellation procedure used on the deepest level of integration refinement provides us with the possibility to extract a parametrization of the boundary. In essence, the immersed boundary is reconstructed on an element-by-element basis by identifying the faces of the integration sub-cells that coincide with the immersed boundary. The collection of sub-cell faces that approximates the immersed boundary provides a piece-wise linear parametrization of this boundary. Using this piece-wise parametrization, quadrature rules can be constructed. Evidently, the refinement parameter $\varrho_{\max}$ controls the accuracy with which the geometry is approximated.

3. Skeleton-stabilized immersed isogeometric analysis for the Navier-Stokes equations

In this section we introduce the skeleton-stabilized immersed isogeometric analysis formulation for the Navier-Stokes equations. We commence with the definition of the topological structures on which this stabilization technique is based, after which we present the two stabilization aspects in our formulation, *viz.* the Ghost penalty stabilization of the velocity components at the cut boundaries, and the pressure stabilization on the skeleton of the background mesh.

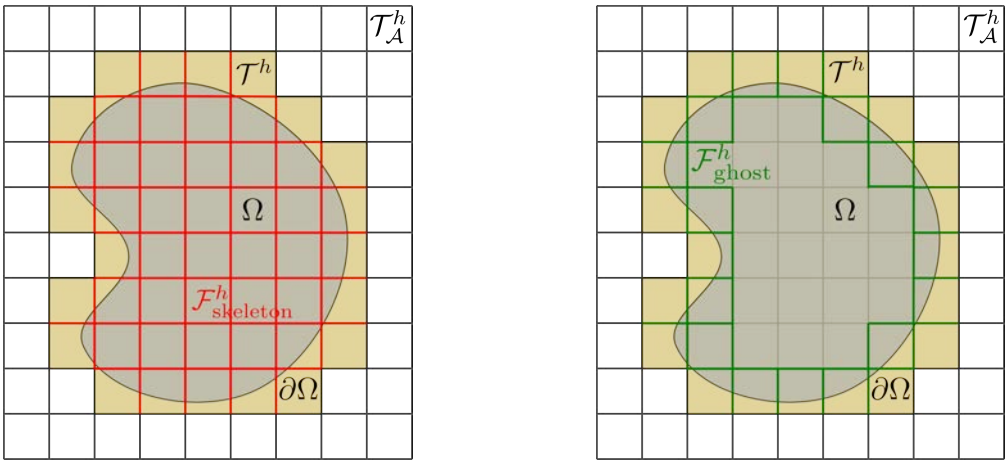

Figure 4: Schemtatic representation of *(a)* the skeleton structure, and *(b)* the ghost interface structure.

3.1. The background mesh: skeleton structure and ghost structure

We consider the background mesh $\mathcal{T}^h$ as defined in Section 2.2. The stabilized formulation presented herein is based on the skeleton of this background mesh, which is defined as

$$\mathcal{F}^h_{\text{skeleton}} = \{\partial K \cap \partial K' \mid K, K' \in \mathcal{T}^h, K \neq K'\}. \tag{9}$$

This skeleton, for which the mesh parameter h is associated with that of the background mesh, is illustrated in Figure 4a. Note that the boundary faces of the mesh $\mathcal{T}^h$ are not a part of this skeleton mesh.

Besides the skeleton structure (9) we also consider that part of the skeleton which coincides with the faces of all cut cells in the domain, to which we refer as the ghost skeleton:

$$\mathcal{F}^h_{\text{ghost}} = \mathcal{F}^h_{\text{skeleton}} \cap \left\{F \mid F \subset \partial K : K \in \mathcal{T}^h, K \cap \partial\Omega \neq \varnothing\right\} \tag{10}$$

This ghost skeleton structure is illustrated in Figure 4b, where the mesh parameter h is still associated with that of the background mesh. Note that this structure does also contain some faces that do not intersect the boundary of the physical domain.

Since we herein consider single patch discretizations of the ambient domain with maximal regularity the basis functions are C^{k-1} continuous over all faces in the skeleton mesh $\mathcal{F}_{\text{skeleton}}$. Therefore, the jumps in the normal derivative up to order $k-1$ of all functions in $\mathcal{S}^k = \text{span}(\mathcal{N}^k)$ vanish:

$$[\![\partial_n^i f]\!]_F = 0, \;\; 0 \leq i \leq k-1, \qquad\qquad \forall f \in \mathcal{S}^k, \tag{11}$$

where the jump operator $[\![\cdot]\!]$ associates to any function f in the broken Sobolev space $\{f \in L^2(\Omega) : f|_K \in H^1(K), \; \forall K \in \mathcal{T}^h\}$ the $L^2(\mathcal{F}^h_{\text{skeleton}})$-valued function:

$$[\![f]\!] = f^+ - f^-$$

The superscripts $(\cdot)^\pm$ refer to the traces of f on the two opposite sides of each face $F \in \mathcal{F}^h_{\text{skeleton}}$, with an arbitrary allocation of $+$ and $-$.

3.2. The Skeleton-stabilized finite cell formulation

In this contribution we study the discretization of problem (1) using identical highest smoothness spline discretizations for the velocity and pressure fields:

$$\boldsymbol{\mathcal{V}}^h := \left[\mathcal{S}^k\right]^d, \qquad\qquad \mathcal{Q}^h := \mathcal{S}^k. \tag{12}$$

The Skeleton-stabilized finite cell formulation for the system (1) reads:

$$\left\{\begin{array}{l} \text{Find } \mathbf{u}^h \in \mathcal{L}(0,T;\boldsymbol{\mathcal{V}}^h) \text{ and } p^h \in \mathcal{L}(0,T;\mathcal{Q}^h), \text{ subject to } \mathbf{u}^h(0) = \mathbf{u}^h_0, \\ \text{such that for almost all } t \in (0,T): \\ \begin{array}{rll} (\partial_t \mathbf{u}^h, \mathbf{w}^h) + c(\mathbf{u}^h;\mathbf{u}^h,\mathbf{w}^h) + a^h(\mathbf{u}^h,\mathbf{w}^h) + s^h_{\text{ghost}}(\mathbf{u}^h,\mathbf{w}^h) + b^h(p^h,\mathbf{w}^h) & = \ell^h_1(\mathbf{w}^h) & \forall \mathbf{w}^h \in \boldsymbol{\mathcal{V}}^h, \\ b^h(q,\mathbf{u}^h) - s^h_{\text{skeleton}}(p^h,q^h) & = \ell^h_2(q^h) & \forall q^h \in \mathcal{Q}^h, \end{array} \end{array}\right. \tag{13}$$

where $\mathbf{u}^h_0$ corresponds to a projection of the initial data on $[\mathcal{S}^k]^d$, and where the linear operators as introduced in the conforming setting in equation (3) are supplemented with additional terms for Nitsche's imposition of the boundary conditions [30]:

$$a^h(\mathbf{u}^h,\mathbf{w}^h) := a(\mathbf{u}^h,\mathbf{w}^h) - 2\mu\left[\langle\nabla^s\mathbf{u}^h\cdot\mathbf{n},\mathbf{w}^h\rangle_{\Gamma_D} + \langle\nabla^s\mathbf{w}^h\cdot\mathbf{n},\mathbf{u}^h\rangle_{\Gamma_D}\right] + \mu\langle\beta h^{-1}\mathbf{u}^h,\mathbf{w}^h\rangle_{\Gamma_D}, \tag{14a}$$

$$b^h(q^h,\mathbf{w}^h) := b(q^h,\mathbf{w}^h) + \langle q^h,\mathbf{w}^h\cdot\mathbf{n}\rangle_{\Gamma_D}, \tag{14b}$$

$$\ell^h_1(\mathbf{w}^h) := \ell_1(\mathbf{w}^h) - 2\mu\langle\nabla^s\mathbf{w}^h\cdot\mathbf{n},\mathbf{g}\rangle_{\Gamma_D} + \mu\langle\beta h^{-1}\mathbf{g},\mathbf{w}^h\rangle_{\Gamma_D}, \tag{14c}$$

$$\ell^h_2(q^h) := \langle q^h\mathbf{n}\cdot\mathbf{g}\rangle_{\Gamma_D}, \tag{14d}$$

where $\langle \cdot, \cdot \rangle_{\Gamma_D}$ denotes the inner product in $L^2(\Gamma_D)$. The two stabilization operators that are appended to the weak form (13) are defined as:

$$s^h_{\text{ghost}}(\mathbf{u}^h, \mathbf{w}^h) := \sum_{F \in \mathcal{F}_{\text{ghost}}} \int_F \widetilde{\gamma} \mu h^{2k-1} [\![\partial^k_n \mathbf{u}_h]\!] \cdot [\![\partial^k_n \mathbf{v}_h]\!] \, \mathrm{ds}, \tag{15a}$$

$$s^h_{\text{skeleton}}(p^h, q^h) := \sum_{F \in \mathcal{F}^h_{\text{skeleton}}} \int_F \gamma \mu^{-1} h^{2k+1} [\![\partial^k_n p^h]\!] [\![\partial^k_n q^h]\!] \, \mathrm{ds}, \tag{15b}$$

where $\widetilde{\gamma}$ and γ denote certain suitable positive stabilization parameters; see Remark 2 below.

The operator $s_{\text{ghost}}(\mathbf{u}^h, \mathbf{w}^h)$ is referred to as the Ghost-penalty operator [28, 29]. This term – which penalizes the (non-vanishing) jump in the k-th order normal derivative on the ghost skeleton, enables scaling of the Nitsche penalty term by the reciprocal mesh size parameter h^{-1} of the *background mesh*, independent of the cut-element configurations. Without the ghost-penalty term, the Nitsche term would have to be based on the reciprocal of the *cut-element* size to ensure stability. However, this would result in configuration-sensitive stability and severe ill-conditioning in critical cases such as sliver cut configurations. The ghost-penalty stabilization hence effectively controls the conditioning of the velocity contributions to the formulation. The condition numbers then scale as in the case of conforming discretizations, and are independent of the configuration of the cut cells [28, 29].

The operator $s_{\text{skeleton}}(p^h, q^h)$ in (13) is referred to as the Skeleton-penalty operator, which was developed for conforming isogeometric discretizations of the unsteady incompressible Navier-Stokes equations in [1], and is applied here without any modification to the immersed setting. This term allows to use identical pairs of spaces for the velocity and pressure fields, as defined in equation (12). It should be emphasized that the skeleton structure is defined not only inside the physical domain but in the whole background mesh. In this way, the pressure-stabilization not only ensures inf-sup stability over the complete domain but also resolves the conditioning issue related to the pressure field in the case of pathological cut configurations.

Remark 1. *We note that the stabilization parameters γ and $\widetilde{\gamma}$, and the viscosity parameter μ, in the operators (15a) and (15b) are kept inside the integrand for the sake of generality. For the simulations considered herein – where we focus on moderate Reynolds numbers flows – these scalings are defined globally. This global scaling may not extend to,* e.g.*, the more general case of convection-dominated flows.*

Remark 2. *The positive parameters γ and $\widetilde{\gamma}$ are selected in an ad hoc manner, where an important guideline is that they should decrease with increasing regularity. In the full regularity setting considered herein, this implies that they decrease with increasing order of the discretization. Since we are using identical highest-regularity B-spline spaces for velocity and pressure fields, we have found that for our test cases acceptable results are generally obtained by assigning the same value to both parameters,* i.e. *$\gamma = \widetilde{\gamma}$.*

Remark 3. *The pressure skeleton-stabilization term and the ghost penalty stabilization term scale differently with the mesh size,* viz. *with h^{2k+1} and h^{2k-1}, respectively. This difference stems from the fact that the velocity field resides in H^1, while the pressure resides in L^2. Note that although we have restricted ourselves herein to regular meshes with global and isotropic size h, there is no fundamental restriction to the application of the formulation (13) in the context of non-uniformly spaced grids.*

The rationale behind the skeleton-stabilized formulation – which for sufficiently smooth velocity and pressure solutions ($\mathbf{u} \in [H^k(\Omega)]^d$ and $p \in H^k(\Omega)$) is consistent with (1) – is that it effectively targets the shortcomings observed using inf-sup stable spaces. The skeleton stabilization operator (15b) is tied to the background domain, in the sense that it is completely independent of the shape and volume fraction of the cut cells it pertains to. As a consequence, the stabilizing effect of the operator does not decrease with decreasing volume fractions. This contrasts the situation in which inf-sup stable pairs are considered, since in that setting the cut cell characteristics have been observed to impact the inf-sup stability [2]. Moreover, the stabilization operator (15b) can be conceived of as a weakly imposed

constraint on the highest-order non-vanishing derivative of the pressure field, which essentially means that it controls the smoothness of the extension of the interior domain into the exterior domain. In [1] we have demonstrated that the operator (15b) is related to the least squares minimization problem for the highest-order derivative jumps. Thereby the operator effectively suppresses oscillations in the pressure field near the immersed boundaries.

4. The algebraic form

Using the B-spline basis functions as defined in Section 2.2, the velocity and pressure field can be expressed as

$$\mathbf{u}^h(\mathbf{x},t) = \sum_{i=1}^{n_u} \mathbf{N}_i(\mathbf{x})\hat{u}_i(t), \qquad p^h(\mathbf{x},t) = \sum_{i=1}^{n_p} N_i(\mathbf{x})\hat{p}_i(t). \tag{16}$$

Note that the basis functions for the velocity field are printed in bold font to indicate that these are vector-valued. The coefficients corresponding to these basis functions are assembled in the vector $\hat{\mathbf{u}}(t) = (\hat{u}_1, \hat{u}_2, \ldots, \hat{u}_{n_u})^T$. The basis functions for the pressure are evidently scalar-valued, with associated coefficient vector $\hat{\mathbf{p}}(t) = (\hat{p}_1, \hat{p}_2, \ldots, \hat{p}_{n_p})^T$. In the absence of constraints, the number of velocity-degrees of freedom, n_u, is d times that of pressure degrees of freedom, n_p.

Consistent with (16) the discrete approximation spaces can be defined as $\boldsymbol{\mathcal{V}}^h = \text{span}\{\mathbf{N}_i\}_{i=1}^{n_u}$ and $\mathcal{Q}^h = \text{span}\{N_i\}_{i=1}^{n_p}$, so that the formulation (13) can be cast into a time-dependent algebraic system of equations of size $n = n_u + n_p$:

$$\begin{cases} \text{For each } t \in (0,T), \text{ find } \hat{\mathbf{u}} = \hat{\mathbf{u}}(t) \in \mathbb{R}^{n_u} \text{ and } \hat{\mathbf{p}} = \hat{\mathbf{p}}(t) \in \mathbb{R}^{n_p}, \text{ given } \hat{\mathbf{u}}(0) = \hat{\mathbf{u}}_0, \text{ such that:} \\ \mathbf{M}\partial_t\hat{\mathbf{u}} + [\mathbf{C}(\hat{\mathbf{u}}) + \mathbf{A} + \mathbf{S}_{\text{ghost}}]\,\hat{\mathbf{u}} + \mathbf{B}^T\hat{\mathbf{p}} = \mathbf{f}_1, \\ \qquad\qquad \mathbf{B}\hat{\mathbf{u}} - \mathbf{S}_{\text{skeleton}}\hat{\mathbf{p}} = \mathbf{f}_2. \end{cases} \tag{17}$$

We employ Crank-Nicolson time integration with Picard iterations to solve this nonlinear algebraic problem in time. See Ref. [1] for details regarding the solution algorithm.

The matrices and vectors in (17) pertaining to the standard volume and boundary surface terms can be expressed in terms of the operators (14) as:

$$C(\hat{\mathbf{u}})_{ij} := c(\hat{\mathbf{u}}; \mathbf{N}_j, \mathbf{N}_i), \tag{18a}$$
$$A_{ij} := a^h(\mathbf{N}_j, \mathbf{N}_i), \tag{18b}$$
$$B_{ij} := b(N_i, \mathbf{N}_j), \tag{18c}$$
$$f_{1,i} := \ell_1^h(\mathbf{N}_i) \tag{18d}$$
$$f_{2,i} := \ell_2(N_i). \tag{18e}$$

The stabilization matrices in (17) pertain to the skeleton and ghost structure of the background mesh, $\mathcal{F}^h_{\text{skeleton}}$ and $\mathcal{F}^h_{\text{ghost}}$, respectively, and hence require data structures to evaluate the jump of high-order derivatives of the basis functions across the background mesh element interfaces through the operators in (15) as:

$$S_{\text{skeleton},ij} = s^h_{\text{skeleton}}(N_j, N_i), \tag{19a}$$
$$S_{\text{ghost},ij} = s^h_{\text{ghost}}(\mathbf{N}_j, \mathbf{N}_i). \tag{19b}$$

Due to the fact that the jump operators on the highest-order derivatives of the B-spline basis functions provide additional connectivity between basis functions, the stabilization matrices (19) have an effect on the sparsity pattern of the algebraic problem. In Figure 5 we present a comparison of the sparsity patterns of the system matrices for the cases of a second-order ($k = 2$) B-spline basis as

considered herein and a second-order ($k = 2$) Lagrange basis (closely resembling the continuous interior penalty method). Note that since both bases are constructed over the same background mesh, the number of Lagrange basis functions is significantly larger (approximately k-times) than the number of B-spline basis functions, by virtue of the fact that, as opposed to Lagrange basis functions, for full-regularity B-splines the number of basis functions does not scale proportionally with the degree of the basis to the power d.

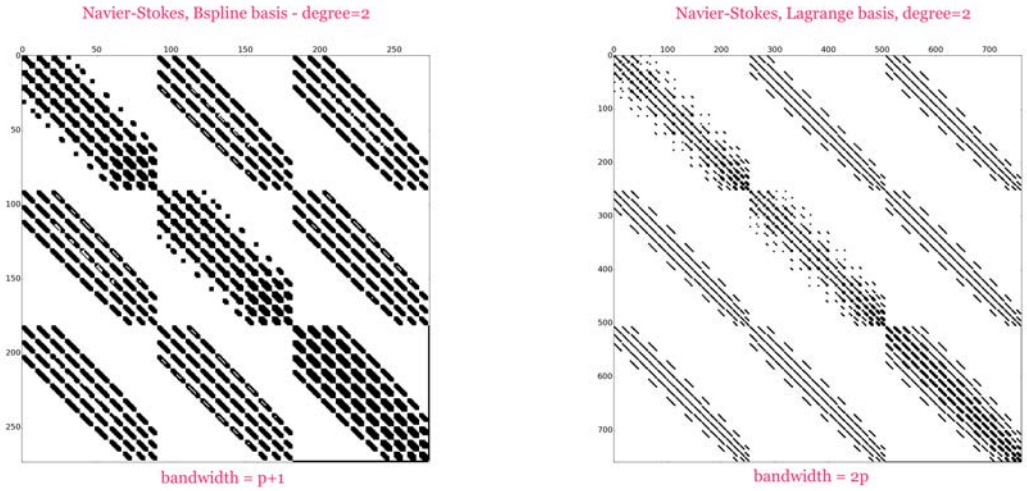

(a) B-spline basis

(b) Lagrange basis

Figure 5: Illustration of the sparsity patterns of the system matrix corresponding to (17) for *(a)* a second-order B-spline basis, and *(b)* a second-order Lagrange basis. The stencil of the B-spline case is smaller than that of the Lagrange case. See Fig. 6 for more elaborations. Note that here both bases are constructed over the same background mesh and therefore result in different numbers of degrees of freedom; the figure sizes are thus not of the same scale.

Inspection of the velocity-velocity and pressure-pressure blocks reveals that the footprint of the stabilization operators have a different effect for the two bases, in the sense that for the $k = 2$ case $2k = 4$ off-diagonal bands are observed for the Lagrange basis, and $k + 1 = 3$ for the B-spline basis. This difference – which becomes more pronounced when the degree k increases – was also observed in the mesh conforming case in Ref. [1], with the difference that in the immersed setting both the velocity and pressure space are stabilized, thereby making the impact of the stabilization operators on the computational effort larger in the immersed setting. Following the arguments in Ref. [1], the difference in number of off-diagonal bands can be explained by comparison of the one-dimensional B-spline and Lagrange bases, as shown for the cubic ($k = 3$) case in Figure 6. This Figure corroborates that in the case of full-regularity B-splines all derivative jumps up to order $k - 1$ vanish across element interfaces, as a result of which only the k-th derivative jump operator impacts the sparsity pattern. The number of off-diagonal bands for the stabilization operators is therefore in this case equal to $k+1$. In contrast, for Lagrange bases, the lower-order derivative jumps are non-vanishing, as a result of which $2k$ off-diagonal bands appear.

5. Numerical simulations

In this section we investigate the numerical performance of the proposed immersed skeleton-stabilized formulation. In all cases, the system (13) is solved using identical highest-regularity B-spline spaces for the approximations of the velocity and pressure fields. Unless stated otherwise, the number of bi-sectioning levels that determines the accuracy of the geometry representation is taken equal to six in the two-dimensional simulations, and equal to five in the three-dimensional case. Evidently, when

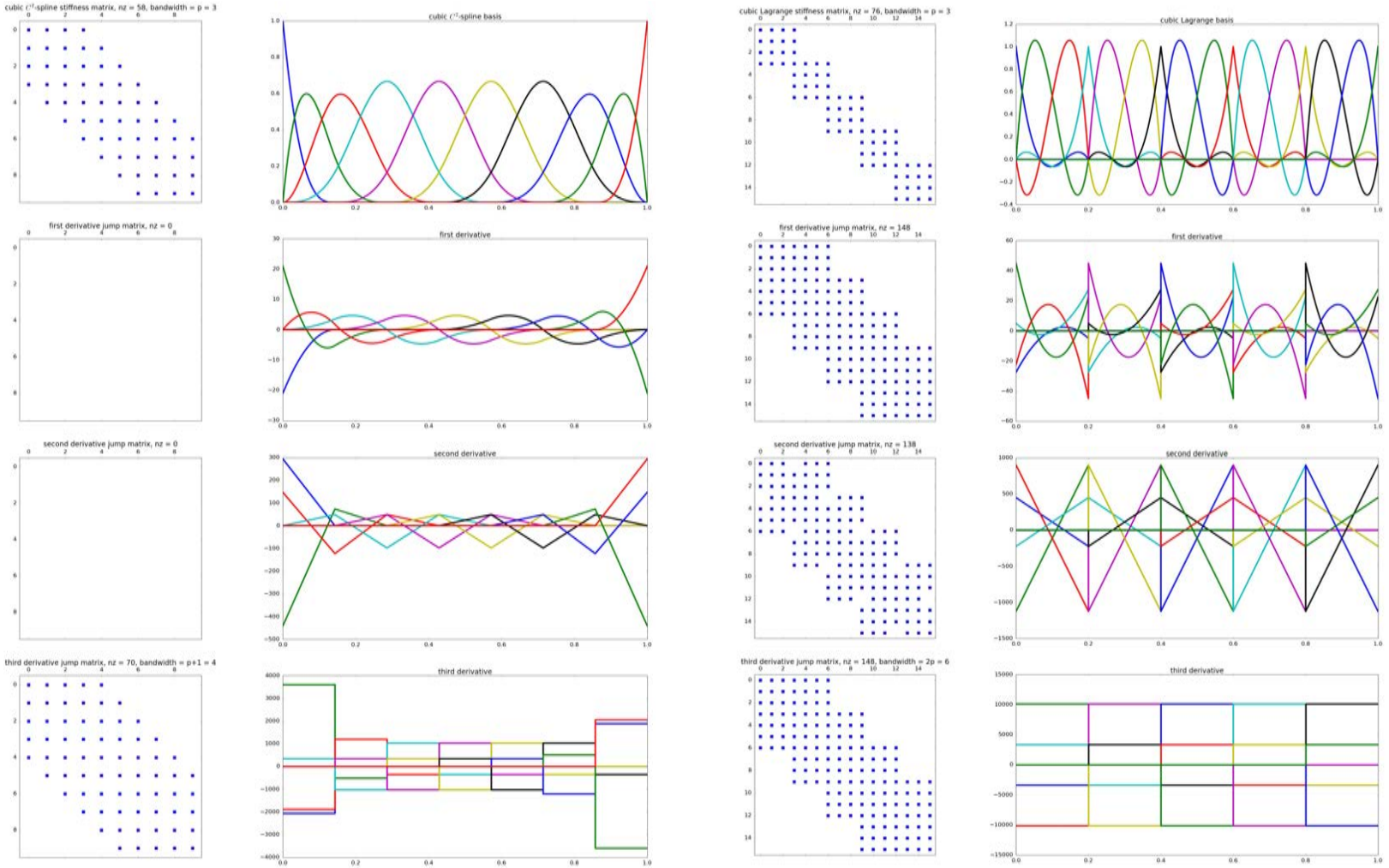

(a) B-spline case

(b) Lagrange case

Figure 6: Comparison of the *(a)* univariate cubic B-spline basis of full regularity, and *(b)* univariate cubic Lagrange basis. Due to the C^{k-1} continuity of the B-spline basis only the k-th derivative jump is non-vanishing, this in contrast to the case of the C^0 continuous Lagrange basis. Moreover, the bandwidth in the B-spline case is $k+1$, much smaller than in the Lagrange case which is $2k$.

studying higher-order approximations, one ideally wants to resolve the geometry as closely as possible. The above-mentioned selected levels of bi-sectioning are chosen such that the simulations remain computationally tractable.

5.1. Steady Navier-Stokes flow in a quarter annulus domain

We consider the steady Navier-Stokes equations on an open quarter-annulus domain

$$\Omega = \left\{(x,y) \in \mathbb{R}^2_{>0} : R_1^2 < x^2 + y^2 < R_2^2\right\},$$

with inner radius $R_1 = 1$ and outer radius $R_2 = 4$; see Figure 7. Dirichlet boundary conditions are prescribed on the entire boundary $\partial\Omega = \Gamma_D$. The body force $\mathbf{f}$ and Dirichlet data $\mathbf{g}$ are selected in accordance with the manufactured solution

$$\begin{aligned} u_1 &= 10^{-6} x^2 y^4 (x^2+y^2-1)(x^2+y^2-16)(5x^4+18x^2y^2-85x^2+13y^4-153y^2+80), \\ u_2 &= 10^{-6} x y^5 (x^2+y^2-1)(x^2+y^2-16)(102x^2+34y^2-10x^4-12x^2y^2-2y^4-32), \\ p &= 10^{-7} xy(y^2-x^2)(x^2+y^2-16)^2(x^2+y^2-1)^2 \exp\left(14(x^2+y^2)^{-1/2}\right), \end{aligned} \tag{20}$$

of problem (1) without the inertia term and with viscosity $\mu = 1$. This manufactured solution is adopted from Refs. [2, 32]. Note that u_1 and u_2 vanish on $\partial\Omega$, and hence $\mathbf{g} = \mathbf{0}$. Moreover, the manufactured pressure solution complies with the zero-average pressure condition $\int_\Omega p = 0$, which is imposed here by means of a Lagrange multiplier.

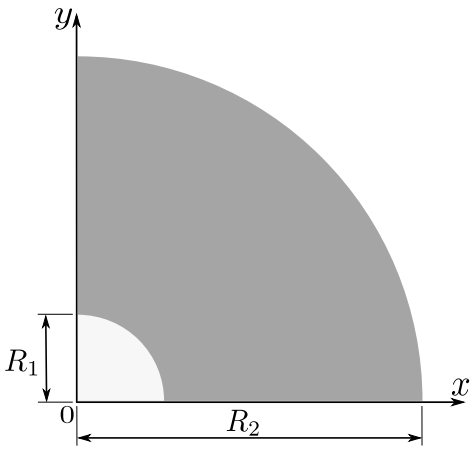

Figure 7: Geometry definition of the quarter-annulus ring problem.

We tested this problem for the Stokes case ($\mu = 0$) in Ref. [2] with different families of inf-sup stable isogeometric spaces. A representative result for that setting is shown in Figure 1a, from which unphysical pressure oscillations in the vicinity of the cut elements are clearly observed. Using inf-sup stable pairs, similar oscillations are also observed in the Navier-Stokes case. In contrast, the pressure field computed using the skeleton-stabilized formulation (13) – illustrated in Figure 8 for the case of quadratic B-splines with a 21×21 elements ambient domain mesh – is free of oscillations. Note that the physical domain is completely immersed in the ambient domain, in the sense that none of the boundaries conform to the background mesh.

In Figure 9 we present mesh convergence results for the proposed stabilized formulation, where a sequence of uniformly refined background meshes is generated starting from the 11×11 elements coarsest ambient domain mesh. The finest level ambient domain mesh contains 176×176 elements. We consider $k = 1, 2, 3$ full-regularity B-splines with stabilization parameters $\gamma = 10$ for $k = 1$, $\gamma = 0.1$ for $k = 2$, $\gamma = 5 \times 10^{-4}$ for $k = 3$ and $\widetilde{\gamma} = 10^{-k-1}$ for all k. We observe optimal rates of convergence of

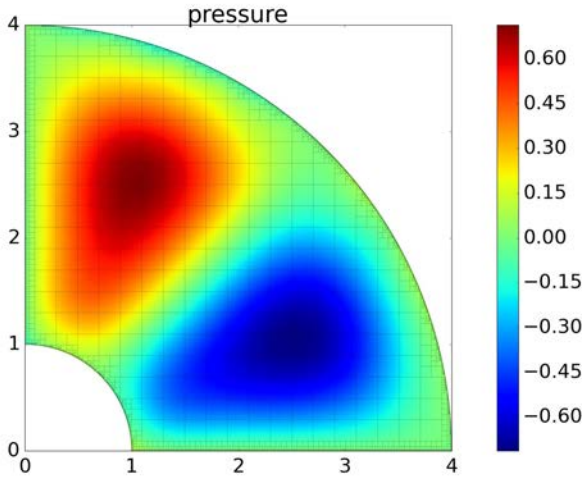

Figure 8: Pressure solution of the steady Navier-Stokes equations with $\mu = 1$, computed using the skeleton-stabilized formulation with quadratic B-splines. The original ambient domain mesh consists of 21×21 elements.

$k+1$ and k for the L^2-norm and H^1-norm of the velocity field, respectively. For the L^2-norm of the pressure we observe the optimal rate of k. It is notable that the convergence behavior of the stabilized formulation considered here is highly regular on all considered meshes, as opposed to the convergence behavior of the non-stabilized FCM formulation; cf. [2].

In Figure 10 we study the solution sensitivity with respect to the skeleton stabilization parameter γ, where the ghost-penalty parameter is fixed at $\widetilde{\gamma} = 5 \times 10^{-3}$. The h-convergence behavior of the solution using C^1-continuous quadratic B-splines is studied for a wide range of stabilization parameters, *viz.* $\gamma \in (5 \times 10^{-5}, 10)$. We observe that the pressure stabilization parameter γ does not affect the accuracy of the velocity field in the L^2-norm and H^1-norm. This behavior is expected, as the Skeleton-penalty term acts only on the pressure field, similar as in the conforming isogeometric analysis setting considered in Ref. [1]. The pressure solution accuracy is affected by the selection of the stabilization parameter, but Figure 10 conveys that the parameter can be selected from a wide range (approximately $\gamma \in (5 \times 10^{-4}, 5 \times 10^{-1})$) with minor influence on the accuracy. The convergence rate remains optimal for all considered choices of the stabilization parameter.

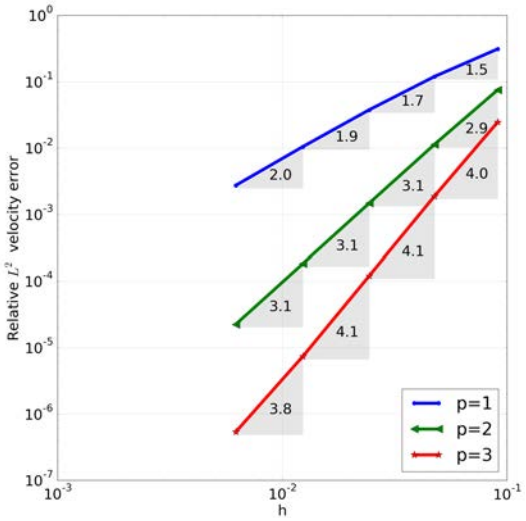

(a) L^2 velocity error

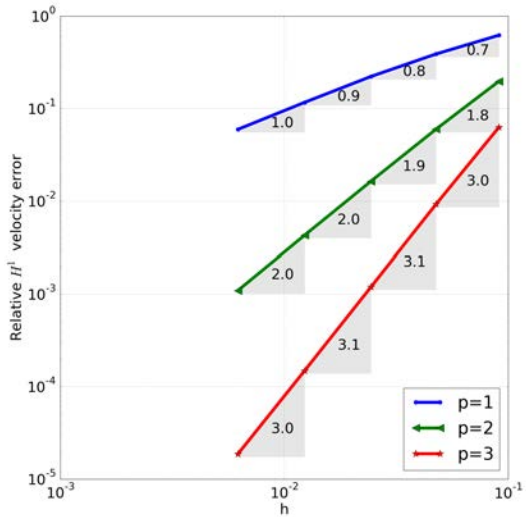

(b) H^1 velocity error

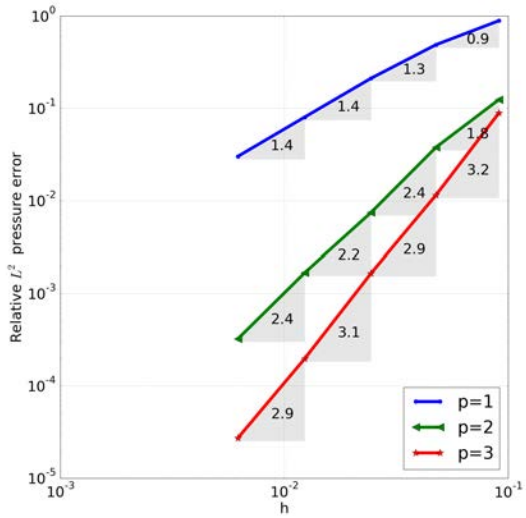

(c) L^2 pressue error

Figure 9: Mesh convergence study of the steady Navier-Stokes equations with $\mu = 1$ in a quarter annulus ring using the skeleton-stabilized formulation with linear, quadratic and cubic full-regularity B-splines.

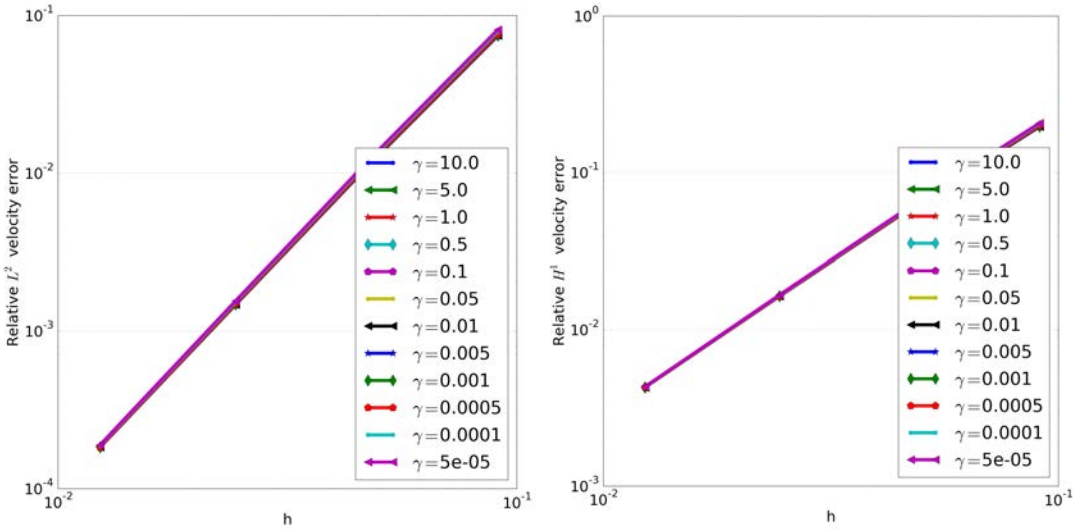

(a) L^2 velocity error

(b) H^1 velocity error

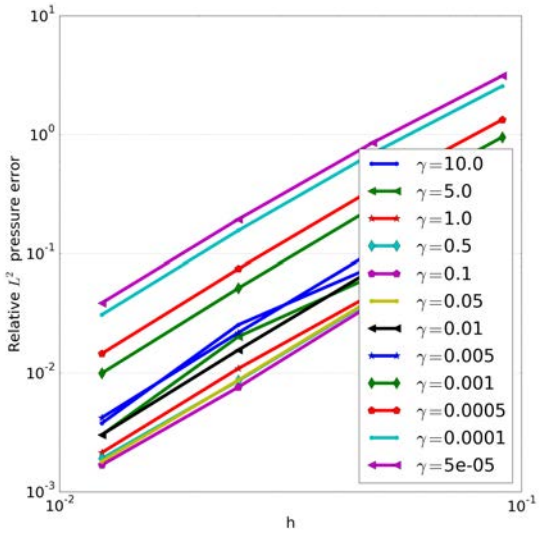

(c) L^2 pressure error

Figure 10: Sensitivity of the quadratic spline approximation of the Navier-Stokes problem with $\mu = 1$ on the quarter annulus ring with respect to the stabilization parameter γ.

5.2. Navier-Stokes flow around a cylinder

We revisit the benchmark problem proposed by Schäfer and Turek [33], which we considered in the mesh-conforming isogeometric analysis setting in Ref. [1]. In this test case a cylinder of radius $R = 0.05\,\mathrm{m}$ is placed in a channel of height $H = 0.41\,\mathrm{m}$ and length $L = 2.2\,\mathrm{m}$. The center of the cylinder is positioned at a horizontal distance of $W = 0.2\,\mathrm{m}$ from the inflow boundary at $x = 0$, and at a vertical distance of $W = 0.2\,\mathrm{m}$ from the bottom channel wall at $y = 0$. Note that the cylinder has a small offset with respect to the center line of the channel, introducing a non-symmetry in the problem. At the inflow boundary the parabolic flow profile

$$\mathbf{u}(0, y) = \begin{pmatrix} 4U_m y(H - y)/H^2 \\ 0 \end{pmatrix}$$

with maximum velocity U_m is imposed. There is no slip at the bottom and top boundaries, as well as along the surface of the cylinder, and a natural boundary condition is used at the outflow boundary ($x = L$). The kinematic viscosity of the fluid is taken as $\mu = 1 \times 10^{-3}\,\mathrm{m}^2/\mathrm{s}$.

We consider the case of $\mathrm{Re} = 20$ – with the Reynolds number defined as $\mathrm{Re} = 2\bar{U}R/\mu$ (with mean inflow velocity $\bar{U} = \frac{2}{3}U_m$ – for which a steady flow is obtained. We consider a sequence of uniform refinements of a relatively coarse ambient domain mesh consisting of 36×22 elements. This coarsest level mesh is a non-uniformly spaced full-regularity B-spline patch, with the knot values selected so that relatively small elements are obtained in the neighborhood of the cylindrical inclusion. The outer boundaries of the ambient domain mesh coincide with the boundaries of the physical domain. The essential boundary conditions are, however, still enforced weakly by Nitsche's method. Figure 11 shows the speed and pressure computed on the three times refined second-order B-spline mesh, which results in a system of $n_{\mathrm{dof}} = 148476$ degrees of freedom. The obtained result is visually in good agreement with the benchmark result, and is free of pressure oscillations near the immersed boundary of the cylinder.

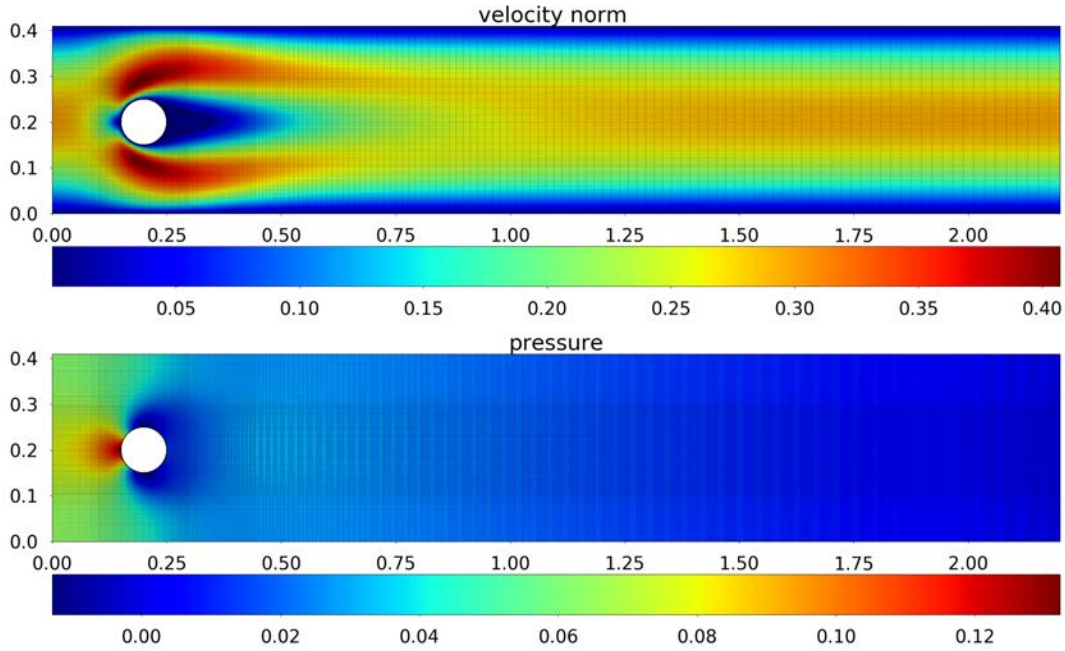

Figure 11: Velocity magnitude (top) and pressure (bottom) solutions of the steady cylinder flow problem using quadratic B-splines with $n_{\mathrm{dof}} = 148476$.

In Table 1 we present the mesh converge results for various quantities of interest, *viz.* the lift and drag coefficients, c_L and c_D, respectively, and the pressure drop over the cylinder, Δp. The drag and lift coefficients are defined as

$$c_D = \frac{F_D}{\rho \bar{U} R} = \frac{\mathcal{R}(\mathbf{u}, p; \boldsymbol{\ell}_1)}{\rho \bar{U} R}, \qquad c_L = \frac{F_L}{\rho \bar{U} R} = \frac{\mathcal{R}(\mathbf{u}, p; \boldsymbol{\ell}_2)}{\rho \bar{U} R},$$

where F_D and F_L are the resultant drag and lift forces acting on the cylinder, which are evaluated weakly as (see *e.g.,* [34–36])

$$\mathcal{R}(\mathbf{u}, p; \boldsymbol{\ell}_i) := (\partial_t \mathbf{u}, \boldsymbol{\ell}_i) + c(\mathbf{u}; \mathbf{u}, \boldsymbol{\ell}_i) + a(\mathbf{u}, \boldsymbol{\ell}_i) - 2\mu \langle \nabla^s \boldsymbol{\ell}_i \cdot \mathbf{n}, \mathbf{u} - \mathbf{g} \rangle_{\Gamma_D} + b(p, \boldsymbol{\ell}_i),$$

with $\boldsymbol{\ell}_i \in [H^1_{0,\partial\Omega\setminus\Gamma}(\Omega)]^d$ and $\boldsymbol{\ell}_i|_\Gamma = -\mathbf{e}_i$, $i = 1, 2$. The pressure drop is defined as

$$\Delta p = p(W/2 - R, W/2) - p(W/2 + R, W/2).$$

Level	n_{dof}	h_{cylinder}	C_D	C_L	Δp
0	2724	0.0142857	5.85317738567	0.009231742514	0.18749814772
1	9984	0.0071428	5.57503959343	0.011002907897	0.12424885895
2	38052	0.0035714	5.57961186549	0.010542479971	0.11504949327
3	148476	0.0017857	5.57989543774	0.010575002816	0.11703150638
Ref. [37]			5.57953523384	0.010618948146	0.11752016697

Table 1: Computed values of the drag and lift coefficients and pressure drop on four refinement levels using the skeleton-stabilized formulation with quadratic B-splines. The mesh resolution in the proximity of the cylinder is indicated by h_{cylinder}, and the total number of degrees of freedom by n_{dof}.

From Table 1 it is observed that on the finest mesh all quantities of interest are in excellent agreement with the benchmark result [37]. We note that – despite the fact that we here have selected the bi-sectioning integration depth to ten – with the higher-order approximation of these quantities of interest we anticipate deterioration of the approximation properties associated with the reduced geometric regularity of the immersed boundary approximation. We expect that the loss of convergence rate especially observed for the drag coefficient can be attributed to this, but further investigation of this aspect is warranted.

5.3. Scan-based analysis of a porous medium flow

To demonstrate the potential of the proposed formulation for geometrically and topologically complex three-dimensional domains, we consider a creeping flow through a porous medium. The porous medium under consideration is made of sintered glass beads. Three-dimensional gray-scale voxel data of the specimen is obtained by a μCT-scanner with a voxel resolution of 25 μm. We here consider a representative domain of $50 \times 50 \times 50$ voxels.

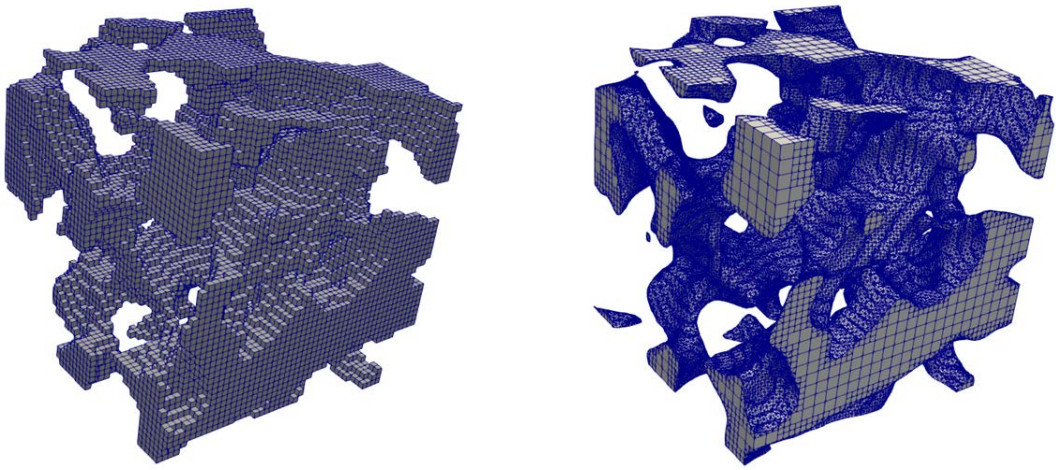

(a) Voxel domain (b) Immersogeometric domain

Figure 12: Two μCT-based geometric models of a sintered glass beads porous medium specimen. The original scan data consists of 125000 gray-scale voxels with a resolution of 25 μm.

In this numerical simulation we compare the immersogeometric approach considered in this work with a voxel-based analysis, which is commonly the method of choice for this type of analyses. The geometric model for the voxel-based analysis is obtained by direct segmentation of the gray-scale data, where all gray-scale values larger than a specified threshold are eliminated from the domain. The voxel model of the segmented void space – with a porosity of 28% – is shown in Figure 12a. The B-spline based finite cell domain is obtained using the procedure proposed in Ref. [21]. First the gray-scale

voxel data is smoothened by convolution of that data with a (second-order) B-spline basis constructed over the voxel grid, an operation that bears resemblance with Gaussian blurring. Then a relatively coarse (second-order) B-spline mesh, *i.e.* consisting of $12 \times 12 \times 12$ elements, is created over the ambient domain matching the scan size, so that the outer boundaries of the pore space reside in the boundaries of the scan domain. The smooth B-spline level set function is then segmented using the bi-sectioning procedure described in Section 2.2 with a bi-sectioning depth of two, where the threshold is calibrated based on the porosity of the voxel model. The corresponding integration mesh – again with a porosity of 28% – is shown in Figure 12b.

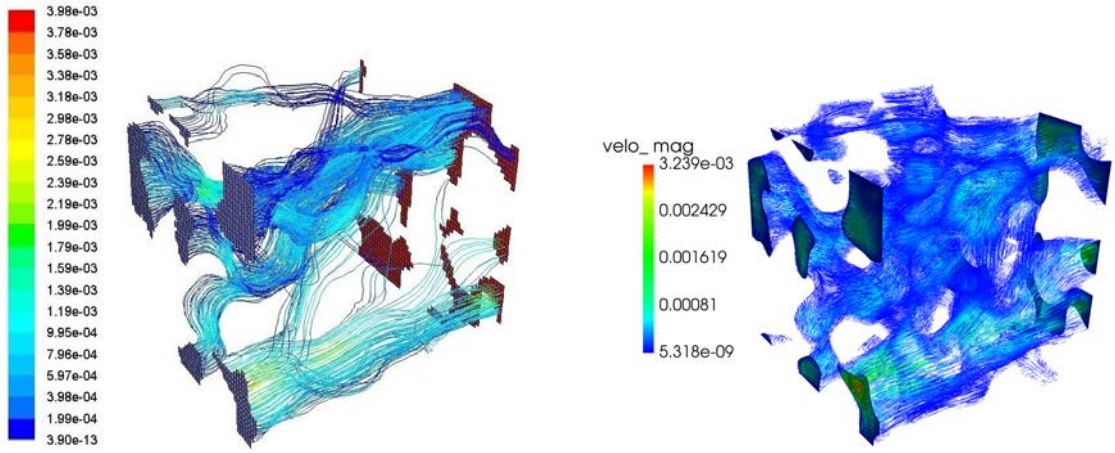

(a) FLUENT: Velocity streamlines

(b) Immersed: Velocity streamlines

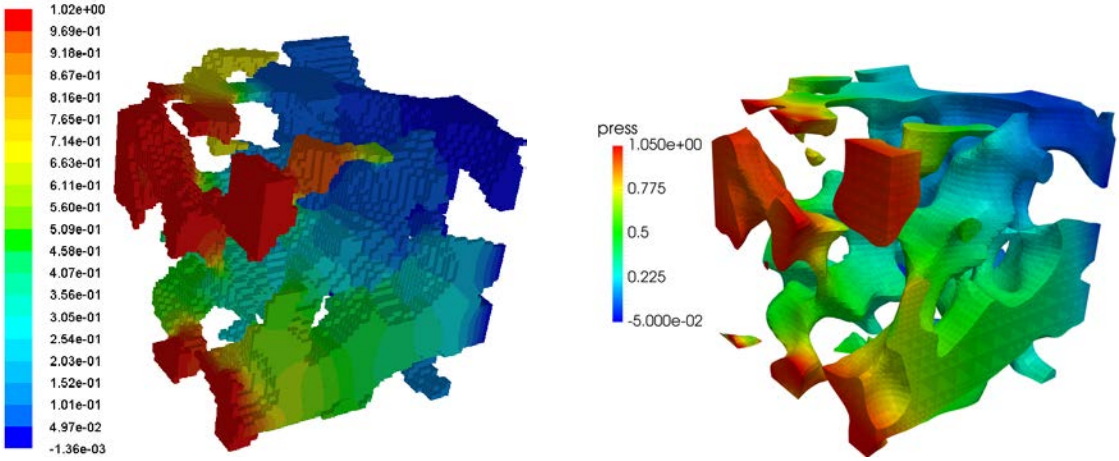

(c) FLUENT: Pressure

(d) Immersed: Pressure

Figure 13: Comparison of the voxel method and immersogeometric analysis results for the sintered glass beads specimen. The units of velocity and pressure are m/s and Pa, respectively.

Comparison of the two geometric models reveals that both models are visually very similar in terms of micro-structural features, which is expected based on the calibrated porosity. Evidently, the surface representation of the models is completely different. Whereas a staircase representation is obtained in the voxel model, a piecewise linear representation of the surface is obtained in the immersogeometric model, where it is noted that the intra-element curvature of the surface is partially recovered by the bi-sectioning operation (*i.e.*, the geometric linearization error is associated with the size of the integration sub-cells, and not with that of the size of the computational background mesh). This difference in surface representation translates directly in a significant difference of the internal surface area, which is equal to $15.5\,\mathrm{mm}^2$ for the voxel model, and to $9.45\,\mathrm{mm}^2$ for the immersogeometric model. Indeed,

a significantly higher surface area is expected in the voxel representation. Adequate representation of the surface is critical in many situations, for example when surface reactions are considered such as in the case of biofilm growth and mineral dissolution/precipitation in porous media [38], or when one is interested in contact line dynamics for multi-phase porous media flows or elasto-capillarity [39–41].

In Figure 13 we compare the analysis results obtained using the two approaches for a creeping flow governed by the Stokes equations with viscosity $\mu = 10^{-3}$ Pa $\cdot$ s. The flow through the porous medium is forced by imposition of a pressure difference of 1 Pa between the inflow (left) and outflow (right) boundaries. All velocity components are zero on the other lateral boundaries, and no slip conditions are imposed on the interior surface. The voxel method results are obtained using FLUENT, which is essentially a finite volume method where the degrees of freedom are closely related with the 35383 pore space voxels. The immersogeometric results are obtained on the above-mentioned mesh using a second-order ($k = 2$) B-spline space, which contains approximately 13 times fewer degrees of freedom than the FLUENT mesh. The skeleton-penalty and ghost-penalty parameters are taken as $\gamma = 10^{-2}$ and $\widetilde{\gamma} = 10^{-4}$, respectively. From Figure 13 we observe the results of both models to be in good correspondence, despite the difference in computational resolution. Let us note that although, because of post-processing artefacts, the streamline patterns for the two simulations are visually distinct, the flow fields are in fact very similar. It is important to note, however, that in terms of computational accuracy the two methods are fundamentally different. In the case of the voxel method, the computational resolution is closely tied to the geometric model, whereas for the immersogeometric approach, the computational mesh resolution can be controlled independent of the geometric model. As demonstrated in Ref. [21] for an elasticity problem, the decoupling of the computational resolution from the geometric model opens the doors to preforming (goal-)adaptive analyses with optimized meshes. In our future work we aim at applying a similar strategy to optimally compute homogenized permeability coefficients. Further optimization of the employed cut cell integration procedures in terms of computational effort – which, per-element, is significantly smaller for the voxel method – is required to allow upscaling to large scale specimens.

6. Conclusions

A stabilized formulation is proposed for the (immersed) finite cell simulation of unsteady incompressible flow problems using identical B-spline bases for the velocity and pressure fields. This formulation extends the developments in Ref. [1], where mesh-conforming isogeometric analysis of incompressible flow problems using identical pressure and velocity bases was considered. The pivotal idea behind the considered stabilization technique – which can be regarded as the isogeometric extension of the continuous interior penalty method – is that the inf-sup condition is bypassed by supplementing a penalty term for basis function derivative jumps across element interfaces, thereby effectively penalizing oscillatory pressure behavior. The mesh-conforming formulation is amended with a ghost-penalty stabilization to resolve ill-conditioning issues associated with small volume fraction cut cells in the immersed finite cell setting. This ghost-penalty term bears close resemblance with the pressure-stabilization operator, but acts on the velocity field in the vicinity of the immersed boundaries only.

An important aspect of this work is that we fully leverage the smoothness properties of the full-regularity B-spline basis functions constructed over the background mesh, in the sense that the stabilization operators only act on the highest-order normal derivatives of the basis functions via their interface jumps. All lower order derivatives vanish as a result of the continuity properties of the B-spline basis. One advantage of this isogeometric approach in comparison to the case of a Lagrange-based analysis is that it only requires a penalty parameter for the highest-order derivative jump. Moreover, the impact of the stabilization term on the sparsity pattern of the system matrix is significantly reduced when full-regularity B-splines are considered instead of Lagrange finite elements. This is an important benefit of the considered isogeometric approach from the perspective of computational effort.

In a series of two-dimensional benchmarks problems we have observed optimal rates of convergence for the L^2 and H^1-norms of the velocity field and the L^2 norm of the pressure field. In comparison to the immersed simulation results based on inf-sup stable isogeometric finite element pairs considered

in Ref. [2], we observe oscillation-free pressure fields near the cut boundaries. As a result, using the skeleton-based stabilization technique considered herein, quantities of interest pertaining to the immersed boundaries can be computed reliably. It is noteworthy, however, that such quantities of interest are affected by the regularity of the immersed boundary representation, which in this work was based on a piece-wise linear representation corresponding to the bi-section based tessellation scheme used to construct quadrature rules for cut cells and their immersed boundaries.

An image-based three-dimensional analysis of a flow through a porous medium was presented, where the geometry is defined by segmentation of the smoothened μCT-scan voxel data. This simulation result demonstrates that the proposed stabilization technique scales to the three-dimensional setting, which opens the door to applying B-spline discretizations to topologically and geometrically complex volumetric domains.

The simulations considered herein were restricted to moderate Reynolds number flows on uniform background meshes. In this setting satisfactory results are obtained when the skeleton penalty parameter and ghost penalty parameter are taken equal. The rates of convergence have been observed to be insensitive to the choice of the penalization parameters for a wide range of considered values. Consistent with observation in the conforming case, the magnitude of the L^2 pressure error is observed to be influenced by the choice of the parameters, but a significant range of parameters exists for which this error is insensitive to the precise values of the parameters. This makes ad hoc selection of the parameters practical. The development of more specific selection criteria – preferably in the form of rigorously derived explicit expressions – is an import aspect of the further development of the proposed simulation framework.

As part of the further development of the mathematical analysis of the proposed formulation, in our future work we aim at obtaining a more fundamental understanding of the influence of geometric irregularities on the approximation quality. In relation to this, we also aim at exploiting the locally refined spline discretizations that can be constructed over the regular background mesh, and to use these refinements in a mesh-adaptive analysis. Extension to convection-dominated problems – which is a non-trivial extension in the sense that an additional convection-stabilization technique must be combined with the stabilization techniques already considered – is also an important topic of further study.

Acknowledgements

We acknowledge the support from the European Commission EACEA Agency, Framework Partnership Agreement 2013-0043 Erasmus Mundus Action 1b, as a part of the *EM Joint Doctorate Simulation in Engineering and Entrepreneurship Development* (SEED). A.R. also acknowledges the support of Fondazione Cariplo - Regione Lombardia through the project "Verso nuovi strumenti di simulazione super veloci ed accurati basati sull'analisi isogeometrica", within the program RST - rafforzamento. C.Q. acknowledges the support of the Darcy Centre of Eindhoven University of Technology and Utrecht University.

We thank Michael Afanasyev from Delft University of Technology for providing the 3D μCT data. The simulations in this work were performed using the open source software package Nutils (www.nutils.org).

References

[1] T. Hoang, C.V. Verhoosel, F. Auricchio, E.H. van Brummelen, and A. Reali. Skeleton-stabilized isogeometric analysis: High-regularity interior-penalty methods for incompressible viscous flow problems. *arXiv preprint arXiv:1711.04910*, 2017.

[2] T. Hoang, C.V. Verhoosel, F. Auricchio, E.H. van Brummelen, and A. Reali. Mixed isogeometric finite cell methods for the stokes problem. *Computer Methods in Applied Mechanics and Engineering*, 316:400 – 423, 2017. Special Issue on Isogeometric Analysis: Progress and Challenges.

[3] T.J.R. Hughes, J.A. Cottrell, and Y. Bazilevs. Isogeometric analysis: CAD, finite elements, NURBS, exact geometry and mesh refinement. *Computer Methods in Applied Mechanics and Engineering*, 194(39-41):4135–4195, 2005.

[4] Y. Bazilevs, L. Beirao da Veiga, J. A. Cottrell, T. J. R. Hughes, and G. Sangalli. Isogeometric analysis: approximation, stability and error estimates for h-refined meshes. *Mathematical Models and Methods in Applied Sciences*, 16(07):1031–1090, 2006.

[5] A. Buffa, C. de Falco, and G. Sangalli. IsoGeometric Analysis: Stable elements for the 2D Stokes equation. *International Journal for Numerical Methods in Fluids*, 65(11-12):1407–1422, 2011.

[6] A. Bressan and G. Sangalli. Isogeometric discretizations of the Stokes problem: stability analysis by the macroelement technique. *IMA Journal of Numerical Analysis*, 33(2):629–651, 2013.

[7] T Rüberg and F Cirak. Subdivision-stabilised immersed B-spline finite elements for moving boundary flows. *Computer Methods in Applied Mechanics and Engineering*, 209:266–283, 2012.

[8] J.A. Evans and T.J.R. Hughes. Isogeometric divergence-conforming B-splines for the Darcy–Stokes–Brinkman equations. *Mathematical Models and Methods in Applied Sciences*, 23(04):671–741, 2013.

[9] J.A. Evans and T.J.R. Hughes. Isogeometric divergence-conforming b-splines for the steady navier–stokes equations. *Mathematical Models and Methods in Applied Sciences*, 23(08):1421–1478, 2013.

[10] J.A. Evans and T.J.R. Hughes. Isogeometric divergence-conforming b-splines for the unsteady navier–stokes equations. *Journal of Computational Physics*, 241:141–167, 2013.

[11] L. Beirao da Veiga, A Buffa, G. Sangalli, and R. Vázquez. Mathematical analysis of variational isogeometric methods. *Acta Numerica*, 23:157–287, 5 2014.

[12] A. Düster, J. Parvizian, Z. Yang, and E. Rank. The finite cell method for three-dimensional problems of solid mechanics. *Computer Methods in Applied Mechanics and Engineering*, 197(4548):3768 – 3782, 2008.

[13] D. Schillinger and E. Rank. An unfitted hp-adaptive finite element method based on hierarchical B-splines for interface problems of complex geometry. *Computer Methods in Applied Mechanics and Engineering*, 200(4748):3358 – 3380, 2011.

[14] E. Rank, M. Ruess, S. Kollmannsberger, D. Schillinger, and A. Düster. Geometric modeling, isogeometric analysis and the finite cell method. *Computer Methods in Applied Mechanics and Engineering*, 249:104–115, 2012.

[15] D. Schillinger, L. Dede, M. A. Scott, J. A. Evans, M. J. Borden, E. Rank, and T. J. R. Hughes. An isogeometric design-through-analysis methodology based on adaptive hierarchical refinement of NURBS, immersed boundary methods, and T-spline CAD surfaces. *Computer Methods in Applied Mechanics and Engineering*, 249:116–150, 2012.

[16] D. Kamensky, M. C. Hsu, D. Schillinger, J. A. Evans, A. Aggarwal, Y. Bazilevs, M. S. Sacks, and T. J. R. Hughes. An immersogeometric variational framework for fluid–structure interaction: Application to bioprosthetic heart valves. *Computer Methods in Applied Mechanics and Engineering*, 2014.

[17] M.-C. Hsu, D. Kamensky, F. Xu, J. Kiendl, C. Wang, M.C.H Wu, J. Mineroff, A. Reali, Y. Bazilevs, and M.S. Sacks. Dynamic and fluid-structure interaction simulations of bioprosthetic heart valves using parametric design with T-splines and Fung-type material models. *Computational Mechanics*, 55:1211–1225, 2015.

[18] D. Schillinger and M. Ruess. The finite cell method: A review in the context of higher-order structural analysis of CAD and image-based geometric models. *Archives of Computational Methods in Engineering*, pages 1–65, 2014.

[19] A. Düster, E. Rank, and B. Szabó. The p-version of the finite element and finite cell methods. *Encyclopedia of computational mechanics. Chichester: John Wiley & Sons*, 2017.

[20] M. Ruess, D. Tal, N. Trabelsi, Z. Yosibash, and E. Rank. The finite cell method for bone simulations: Verification and validation. *Biomechanics and Modeling in Mechanobiology*, 2011.

[21] C.V. Verhoosel, G.J. van Zwieten, B. van Rietbergen, and R. de Borst. Image-based goal-oriented adaptive isogeometric analysis with application to the micro-mechanical modeling of trabecular bone. *Computer Methods in Applied Mechanics and Engineering*, 284:138 – 164, 2015.

[22] E. Burman and P. Hansbo. Edge stabilization for the generalized stokes problem: a continuous interior penalty method. *Computer methods in applied mechanics and engineering*, 195(19):2393–2410, 2006.

[23] E. Burman and P. Hansbo. Fictitious domain methods using cut elements: Iii. a stabilized nitsche method for stokes problem. *ESAIM: Mathematical Modelling and Numerical Analysis*, 48(3):859–874, 2014.

[24] B. Schott and W.A. Wall. A new face-oriented stabilized xfem approach for 2d and 3d incompressible navier–stokes equations. *Computer Methods in Applied Mechanics and Engineering*, 276:233–265, 2014.

[25] A. Massing, M.G. Larson, A. Logg, and M.E. Rognes. A stabilized nitsche fictitious domain method for the stokes problem. *Journal of Scientific Computing*, 61(3):604–628, 2014.

[26] J. Guzmán and M. Olshanskii. Inf-sup stability of geometrically unfitted stokes finite elements. *arXiv preprint arXiv:1605.09681*, 2016.

[27] A. Massing, B. Schott, and W.A. Wall. A stabilized nitsche cut finite element method for the oseen problem. *arXiv preprint arXiv:1611.02895*, 2016.

[28] E. Burman. Ghost penalty. *Comptes Rendus Mathematique*, 348(21-22):1217–1220, 2010.

[29] E. Burman and P. Hansbo. Fictitious domain finite element methods using cut elements: Ii. a stabilized nitsche method. *Applied Numerical Mathematics*, 62(4):328–341, 2012.

[30] J. Nitsche. Uber ein Variationsprinzip zur Losung von Dirichlet-Problemen bei Verwendung von Teilraumen, die keinen Randbedingungen unterworfen sind. *Abhandlungen aus dem Mathematischen Seminar der Universitat Hamburg*, 36(1):9–15, 1971.

[31] L. A. Piegl and W. Tiller. *The NURBS book*. Springer Verlag, 1997.

[32] F. Auricchio, L. Beirao da Veiga, A. Buffa, C. Lovadina, A. Reali, and G. Sangalli. A fully "locking-free" isogeometric approach for plane linear elasticity problems: a stream function formulation. *Computer methods in applied mechanics and engineering*, 197(1):160–172, 2007.

[33] M. Schäfer, S. Turek, F. Durst, E. Krause, and R. Rannacher. Benchmark computations of laminar flow around a cylinder. In *Flow simulation with high-performance computers II*, pages 547–566. Springer, 1996.

[34] E.H. van Brummelen, K.G. van der Zee, V.V. Garg, and S. Prudhomme. Flux evaluation in primal and dual boundary-coupled problems. *Journal of Applied Mechanics*, 79(1), 2012.

[35] M. G. Larson and A. Massing. L^2-error estimates for finite element approximations of boundary fluxes. *arXiv preprint arXiv:1401.6994*, 2014.

[36] M. Giles, M.G. Larson, J.M. Levenstam, and E. Süli. Adaptive error control for finite element approximations of the lift and drag coefficients in viscous flow. 1997.

[37] G. Nabh. *On high order methods for the stationary incompressible Navier-Stokes equations*. Interdisziplinäres Zentrum für Wiss. Rechnen der Univ. Heidelberg, 1998.

[38] C. Qin, S.M. Hassanizadeh, and A. Ebigbo. Pore-scale network modeling of microbially induced calcium carbonate precipitation (micp): Insight into scale dependence of biogeochemical reaction rates. *Water Resources Research*, 52, 2016.

[39] E.H. van Brummelen, M. Shokrpour Roudbari, and G.J. van Zwieten. Elasto-capillarity simulations based on the Navier-Stokes-Cahn-Hilliard equations. In *Advances in Computational Fluid-Structure Interaction and Flow Simulation*, Modeling and Simulation in Science, Engineering and Technology, pages 451–462. Birkhäuser, 2016.

[40] J. Bueno, H. Casquero, Y. Bazilevs, and H. Gomez. Three-dimensional dynamic simulation of elastocapillarity. *Meccanica*, pages 1–17, 2017.

[41] E.H. van Brummelen, M. Shokrpour Roudbari, G. Simsek, and K.G. van der Zee. *Fluid Structure Interaction*, volume 20 of *Radon Series on Computational and Applied Mathematics*, chapter Binary-fluid–solid interaction based on the Navier–Stokes–Cahn–Hilliard Equations. De Gruyter, 2017.